

Spin-polarized Correlated Insulator and Superconductor in Twisted Double Bilayer Graphene

Xiaomeng Liu^{1†*}, Zeyu Hao^{1†}, Eslam Khalaf¹, Jong Yeon Lee¹, Kenji Watanabe², Takashi Taniguchi², Ashvin Vishwanath¹ & Philip Kim^{1*}

¹*Department of Physics, Harvard University, Cambridge, Massachusetts 02138, USA*

²*National Institute for Material Science, 1-1 Namiki, Tsukuba 305-0044, Japan*

†*Theses authors contribute equally to this work.*

Ferromagnetism and superconductivity typically compete with each other¹ **since the internal magnetic field generated in a magnet suppresses the formation of spin-singlet Cooper pairs in conventional superconductors**². **Only a handful of ferromagnetic superconductors are known in heavy fermion systems**^{3–5}, where many-body electron interactions promoted by the narrow energy bands play a key role in stabilizing these emergent states. Recently, interaction-driven superconductivity and ferromagnetism have been demonstrated in different density regimes of flat bands enabled by graphene moire superlattices^{6–9}, as separate phenomena. Combining superconductivity and magnetism in a single ground state may lead to more exotic quantum phases. Here, employing van der Waals heterostructures of twisted double bilayer graphene (TDBG), we realize a flat electron band that is tunable by perpendicular electric fields. Similar to the magic angle twisted bilayer graphene, TDBG exhibits energy gaps at the half and quarter filled flat bands, indicating the emergence of correlated insulating states. We find that the gaps of these insulating states increase with in-plane magnetic field, suggesting a ferromagnetic order. Upon doping the ferromagnetic half-filled insulator, superconductivity appears with a critical temperature controlled by both density and electric fields. We observe that the in-plane magnetic field enhances the superconductivity in the low field regime, suggesting spin-polarized electron pairing. Spin-polarized superconducting states discovered in TDBG provide a new route to engineering interaction-driven topological superconductivity¹⁰.

Moire superlattices of two dimensional (2D) van der Waals (vdW) materials provide a new scheme for creating correlated electronic states. By stacking atomically thin vdW layers with a controlled twist angle θ between them, the size of the moire unit cell can be tuned ¹¹⁻¹³. In particular, in twisted bilayer graphene (TBG), the weak interlayer coupling can open up energy gaps at the boundary of the mini-Brillouin zone, which modifies the energy band-width of the coupled system. Theoretically, it has been predicted that around $\theta \approx 1.1^\circ$ (the so-called magic-angle (MA)), the interlayer hybridization induces isolated flat bands with drastically reduced bandwidth and enhanced density of states ¹⁴. Recent experiments performed in MA-TBG indeed confirmed the appearance of correlated insulating states associated with the flat band ⁶. Surprisingly, it has also been discovered that upon doping the half-filled insulator in MA-TBG, superconductivity appears, phenomenologically resembling high temperature cuprate superconductors whose undoped parent compounds are Mott insulators ¹⁵.

In TBG, the value of the MA is governed by the individual layer band structure and interlayer coupling strength. While the mechanism of superconductivity in the moire superlattice is under debate ¹⁶⁻²¹, continuous tuning of the superlattice band structure across the MA condition will provide experimental control to elucidate the correlated electronic states. However, to date, such an experimental control is largely achieved by fabricating samples with different twist angles, and only very limited tunability has been demonstrated in TBG by application of hydrostatic pressure ^{8,22}. In ABC trilayer graphene/hBN superlattice, electric field was shown to modulate the correlated insulator gap ²³, opening up the possibility of easy tuning of the moire flat band with electric field. Here, we demonstrate electric field-tunable moire flat bands in twisted double bilayer graphene (TDBG), consisting of two Bernal-stacked bilayer graphene sheets misaligned with a twist angle (Fig. 1a). Unlike monolayer graphene, the band structure of Bernal-stacked bilayer graphene itself can be tuned by a perpendicular displacement field D ²⁴. As $|D|$ increases, the parabolic band touching at charge neutrality of bilayer graphene opens up a gap and the bottom (top) of the conduction (valance) band develops a shallow Mexican-hat energy dispersion distorted by trigonal warping ²⁵. The gap in the bilayer graphene can be as big as 200 meV for large $|D|$ before the gate dielectric breaks down ²⁶. In TDBG, where two bilayers are stacked, this addi-

tional band adjustment changes the energy dispersion of each constituent bilayer, allowing a new experimental knob to tune the flat band condition. Fig. 1c shows rearranged moire band structures computed at finite D using the continuum model approximation^{14,27-29}. We find that well-isolated narrow conduction band can appear in a range of twist angle θ , where the inter-band energy gaps and bandwidth can be controlled by the displacement field (see Supplementary Information (SI) S1 for detail).

We fabricated TDBG devices by tearing and stacking Bernal stacked bilayer graphene^{30,31}. Separated by hexagonal boron nitride from TDBG, top and bottom graphite gates with voltages V_{TG} and V_{BG} are used to control the density of electrons n and D independently: $n = C_{TG}V_{TG} + C_{BG}V_{BG}$, $D = (C_{TG}V_{TG} - C_{BG}V_{BG})/2$, where C_{TG} (C_{BG}) is the capacitance between TDBG and the top (bottom) gate. Fig. 1d shows the four-probe resistivity ρ measured in the TDBG with $\theta = 1.33^\circ$ as a function of V_{TG} and V_{BG} at temperature $T = 1.6$ K. Generally, ρ exhibits several insulating states where the corresponding conductance $\sigma = \rho^{-1}$ vanishes as temperature T decreases (Fig. 1g), suggesting gap opening at the Fermi level of the system. Some insulating regions identified in Fig. 1d can be explained in the single particle band structure described in Fig. 1c. For example, we find that the charge neutral point (CNP) is gapless at $D = 0$ but a gap opens up above finite displacement field D_1 . Similarly, at full moire band filling $n = \pm n_s$, where n_s is the density corresponding to four electrons per moire unit cell considering spin and valley degeneracy, energy gaps $\Delta_{\pm n_s}$ are present within displacement field ranges $|D| < D_2^\pm$. The ranges of D_2^\pm are different in the conduction band (+) and valance (-) band, due to the lack of electron-hole symmetry of TDBG. We further confirm the narrowness of the band by estimating the effective cyclotron mass m^* from the temperature dependent magnetoresistance oscillation measurement (see SI, S3.3). Fig. 1f shows that $m^* \approx 0.2m_e$ for the first valance band (v_1) and $\sim 0.4m_e$ for the first conduction band (c_1), where m_e is the bare electron mass. Considering the effective mass of Bernal-stacked bilayer graphene is $\approx 0.04m_e$ ³², the experimentally observed large m^* indicates an order of magnitude narrower band width than folded bilayer graphene bands especially for c_1 band in this regime of gate configurations. Calculations based on a continuum model (Fig. 1c) demonstrate the existence of a isolated flat band at this twist angle under displacement field (theo-

retical bandwidth is around $10\sim 15\text{meV}$), providing a qualitative agreement with the experimental results (SI, S1).

In the single particle band structure, we expect a narrow but uninterrupted spectrum within the lowest moire conduction band (c_1), separated by band gaps from both the valance band (v_1) and higher conduction band (c_2) when $D_1 < |D| < D_2^+$. However, we observe development of well-defined insulating behavior at half-filling $n = n_s/2$ (Fig. 1d, f). The onset of this insulating state coincides with D_1 but this state ends well before D reaches D_2^+ , suggesting both the isolation and flatness of the band are responsible for creating the observed correlated gap (SI, S2). The absence of correlated insulating behavior in the hole-doped regime in similar experimental conditions can also be explained by the wider band width in the moire valance band v_2 compared to that of c_1 (SI, S1).

We measure the size of the gaps from temperature-dependent activating behavior of ρ (Fig. 1g inset). For $\theta = 1.33^\circ$ TDBG, the half-filled insulator is robust with an energy gap of $\Delta_{n_s/2} = 3\text{ meV}$ and persists up to a perpendicular magnetic field $B_\perp \approx 7\text{ T}$ (SI, S3.2). Since c_1 band is spin and valley degenerate in a single particle picture, the correlated insulator we observed in the half-filling is likely polarized in the spin-valley space. Applying in-plane magnetic field B_\parallel can probe the spin structure of the state without significant coupling to the valley. In MATBG, it has been shown that B_\parallel reduces $\Delta_{n_s/2}$, suggesting that the half-filled insulator is a spin-unpolarized state. Fig. 1e shows the change of ρ as a function of B_\parallel in our TDBG sample. We find that the half-filled insulating state becomes more insulating as B_\parallel increases (Fig. 1g inset) and the displacement field range where the half-filled insulator spans also enlarges (Fig. 1e). More quantitatively, we find the activation gap $\Delta_{n_s/2}$ increases with B_\parallel for the half-filled insulating state. The growth of $\Delta_{n_s/2}$ roughly follows the Zeeman energy scale $g\mu_B B_\parallel$ where μ_B is the Bohr magneton and the effective g-factor $g = 2$ (dotted line in Fig. 1h). This observation is consistent with a picture where the occupied states (half of the states in c_1) are spin-polarized along the direction of the external magnetic field. The unoccupied states then carry the opposite spin, separated by a spontaneous ferromagnetic gap. Considering spin-1/2, the Zeeman term lowers the

energy of filled states $\Delta E_\downarrow = -g\mu_B B/2$, while boosting the energy of empty states with opposite spins by $\Delta E_\uparrow = g\mu_B B/2$, pushing the two bands further apart and enhancing the gap (as illustrated by Fig. 1h insets).

Applying B_{\parallel} also induces additional correlated insulating states at quarter-filling ($n = \frac{1}{4}n_s$) and three-quarter-filling ($n = \frac{3}{4}n_s$), which are absent at zero magnetic field. As shown in the upper panel of Fig. 1e, these insulating states are more fragile than the half-filled insulating state as they are stabilized in narrower displacement field ranges. The quarter-filled insulating gap opens at $B_{\parallel} \approx 4$ T and increases as B_{\parallel} increases (Fig. 1h). Considering that the full bands are spin and valley degenerate, these quarter-filled (or quarter-empty) states are presumably polarized in spin-valley phase space. While the details of the mechanism and the texture of the spin/ valley structure is yet to be investigated, the fact that the energy gaps corresponding to these states increase approximately with $g\mu_B B_{\parallel}$ suggests that the corresponding insulating states are spin polarized as illustrated in the upper inset of Fig. 1h.

Fig. 2a shows ρ measured in another sample with smaller twist angle $\theta = 1.24^\circ$. Here, again, the half-filled insulating regime is found at finite displacement fields. However, in this smaller angle, we find the correlated insulating behavior is weaker with a much smaller energy gap ($\Delta_{n_s/2} = 0.3$ meV) than that of the $\theta = 1.33^\circ$ sample. Despite an order of magnitude reduction compared to the previous sample, $\Delta_{n_s/2}$ increases with increasing B_{\parallel} closely following the Zeeman energy, $g\nu_B B_{\parallel}$, indicating spin-polarization of the c_1 band (Fig. 3b). We also note that the single particle gap Δ_{n_s} between c_1 and c_2 decreases linearly with Zeeman energy with g-factor of 2 (Fig. 3b). This behavior can be explained by splitting and down-shifting of spin-aligned states in c_2 and up-shifting of spin-anti-aligned states in c_1 , providing additional confirmation of spin-polarization of the c_1 band, as illustrated in Fig. 3b inset.

Upon doping electrons in the half-filled insulator, we discover superconductivity in the $\theta = 1.24^\circ$ sample. Fig. 2b shows the temperature dependent ρ measured at several different gate configurations presented in Fig. 2a with the same color coordination. We find that the su-

perconductivity appears within the upper right side of the half-filled insulator region in Fig. 2a, surrounded by a half-circle ring of high ρ values ($\gtrsim 0.5$ k Ω). In the center of this superconducting half-circle region ($D = D_m \approx 0.38$ V/nm and $n = n_m \approx 2n_s/3$), the observed superconductivity is strongest: $\rho(T)$ rapidly drops around $T = 6$ K and reaches zero at $T \approx 3.5$ K (black line in Fig. 2b). At finite bias, a typical current-voltage (I - V) curve for superconductors is observed (Fig. 2c). By fitting the I - V curves with $V \propto I^\alpha$, we extract the Berezinskii-Kosterlitz-Thouless (BKT) transition temperature $T_{BKT} = 3.5$ K, defined at $\alpha(T) = 3$ (Fig. 2c inset)².

We find that the superconductivity in TDBG sample can be tuned by both density and displacement field. In Fig. 2d, we show $\rho(T)$ as a function of n at a fixed $D = D_m$. A dome region of superconductivity can be recognized next to the half-filled insulator ($n = n_s/2$), similar to the one seen in MA-TBG, but with a much larger temperature scale. At the optimal doping ($n = n_m$), the superconductivity observed in TDBG also weakens away from the optimal displacement field D_m . In Fig. 2b inset, $\rho(D, T)$ exhibits a dome-like domain of superconducting region in the (D, T) plane. Inside of this superconducting dome region, we find that the differential resistance dV/dI responds sharply to increasing temperature, magnetic field and drive current, which are signatures of superconductivity. Outside of the superconducting region, however, we do not observe sharp temperature transition nor typical superconducting I - V behavior. The low resistance or even negative resistance that appeared at some gate configurations (as shown in Fig. 3a) is possibly due to the mesoscopic ballistic transport (see SI S5.2).

On applying perpendicular magnetic fields B_\perp , the superconductivity is suppressed above $B_\perp^c = 0.1$ T (Fig. 2e). For $B_\perp \gg B_\perp^c$, we observe that $\rho(n, B_\perp)$ exhibits Shubnikov-de Haas (SdH) quantum oscillations at temperatures above the superconducting dome region where the superconductivity was destroyed. The corresponding Landau fan can be traced to the electron filling of the half-filled insulating state. This observation indicates that the TDBG superconductivity is closely linked with the ferromagnetic half-filled insulating states. Thus the Cooper pairs responsible for the superconductivity are likely built upon a Fermi surface that is derived from the doped ferromagnetic insulator.

In order to explore the spin structure of the TDBG superconductivity, we investigate the behavior of $\rho(T)$ as a function of B_{\parallel} . Fig. 3a shows that the superconducting dome in (n, B_{\parallel}) plane with the maximum critical parallel magnetic field $B_{\parallel}^c \approx 1$ T. The salient experimental feature is the B_{\parallel} dependence of the superconducting state below the critical field B_{\parallel}^c . Fig. 3c shows ρ at the optimal superconducting state (n_m, D_m) measured as a function of T and B_{\parallel} . In this optimal superconducting state, ρ vanishes critically as T and B_{\parallel} decreases. We use a phenomenological definition of the critical temperature with the 50% transition point defined as $T_{50\%}$. Interestingly, $T_{50\%}(B_{\parallel})$ follows a non-monotonic behavior. In particular, $T_{50\%}$ increases as B_{\parallel} increases from 0 to ~ 0.3 T before it decreases for $B_{\parallel} > 0.3$ T. We also note that under large in-plane magnetic fields $B_{\parallel} > 1.5$ T, an insulating behavior is recognized from both the temperature dependence in Fig. 3c ($T < 4$ K) and high resistivity shown in Fig. 3a, where the normal state under strong magnetic field tends to be insulating (see SI S5.4).

Our observation of the strengthening of superconductivity with increasing magnetic field is extremely unusual within the framework of spin-singlet s-wave superconductivity. Only a handful of examples of related experimental observations are reported in superconductivity based on heavy fermions ³⁻⁵ and topological systems ^{33,34}, where complex spin textures of electronic systems are involved. To further quantify the enhanced superconductivity at the low B_{\parallel} regime, we performed I - V characterization at the optimal gate configuration (n_m, D_m) as a function of B_{\parallel} and T to obtain T_{BKT} . Similar to $T_{50\%}$ above, $T_{BKT}(B_{\parallel})$ also exhibits a non-monotonic behavior as shown in Fig. 3c (black circles). At low magnetic regime, particularly, we find $k_B \Delta T_{BKT} \approx g \mu_B |B_{\parallel}|$, developing a sharp cusp at $B_{\parallel} = 0$. This is in reminiscent of the magnetic field dependence of the transition temperature in superfluid He_3 where spin triplet pairing is obtained ³⁵. The underlying reason for this linear increase in T_{BKT} is the increase in the density of states of the favorably aligned spins due to Zeeman splitting. In general, the resulting linear coefficient depends on details such as Fermi energy and magnetic susceptibility ³⁵. The measured value of this coefficient $\approx g \mu_B / k_B$, which is seemingly independent of these details, hints at the existence of a proximate ferromagnetic quantum critical point ³⁶.

The increase of T_{BKT} with B_{\parallel} suggests the Cooper pairs responsible for the TDBG superconductivity are likely to be spin-polarized. Adding the requirement of overall anti-symmetric wavefunction for electron pairs, the orbital component (including valley) of the Cooper pair wavefunction thus has to be anti-symmetric. One possible scenario for such a state is illustrated in Fig. 3d, where the Cooper pairs form between Fermi surfaces with the same spin (spin-triplet) and opposite valley. If the wavefunction is a valley singlet, then the extended spatial wavefunction should be s- or d-wave. Conversely, with valley-triplet pairing, p-wave superconductivity is then expected. In this ferromagnetic superconductor, parallel magnetic field enlarges the majority spin Fermi surface, and strengthens the superconductivity, inducing the change of critical temperature $\Delta T_c \propto B$. The eventual destruction of superconductivity at high magnetic field can result from the following mechanism. Magnetic flux in between layers leads to a momentum shift which has opposite sign in the two valleys, thereby bringing the two pairing Fermi surfaces out of alignment. The latter effect is expected to reduce the critical temperature, $\Delta T_c \propto -B^2$ ³⁶. Alternatively, if the ferromagnetic pairing is caused by spin fluctuations, as suggested in the heavy fermion metals^{3–5}, strong parallel magnetic field can suppress the superconductivity by suppressing spin fluctuations³⁷.

1. Khan*, H. R. & Raub, C. J. Ferromagnetism and Superconductivity. *Annual Review of Materials Science* **15**, 211–226 (1985).
2. Tinkham, M. *Introduction to Superconductivity* (Courier Corporation, 2004).
3. Saxena, S. S. *et al.* Superconductivity on the border of itinerant-electron ferromagnetism in UGe₂. *Nature* **406**, 587–592 (2000).
4. Aoki, D. *et al.* Coexistence of superconductivity and ferromagnetism in URhGe. *Nature* **413**, 613–616 (2001).
5. Huy, N. T. *et al.* Superconductivity on the Border of Weak Itinerant Ferromagnetism in UCoGe. *Physical Review Letters* **99** (2007).
6. Cao, Y. *et al.* Correlated insulator behaviour at half-filling in magic-angle graphene superlattices. *Nature* **556**, 80–84 (2018).

7. Cao, Y. *et al.* Unconventional superconductivity in magic-angle graphene superlattices. *Nature* **556**, 43–50 (2018).
8. Yankowitz, M. *et al.* Tuning superconductivity in twisted bilayer graphene. *Science* **363**, 1059–1064 (2019).
9. Sharpe, A. L. *et al.* Emergent ferromagnetism near three-quarters filling in twisted bilayer graphene. *arXiv:1901.03520 [cond-mat]* (2019). ArXiv: 1901.03520.
10. Bernevig, B. A. & Hughes, T. L. *Topological insulators and topological superconductors*. URL <https://press.princeton.edu/titles/10039.html>.
11. Dean, C. R. *et al.* Hofstadters butterfly and the fractal quantum Hall effect in moir superlattices. *Nature* **497**, 598–602 (2013).
12. Ponomarenko, L. A. *et al.* Cloning of Dirac fermions in graphene superlattices. *Nature* **497**, 594–597 (2013).
13. Hunt, B. *et al.* Massive Dirac Fermions and Hofstadter Butterfly in a van der Waals Heterostructure. *Science* **340**, 1427–1430 (2013).
14. Bistritzer, R. & MacDonald, A. H. Moire bands in twisted double-layer graphene. *Proceedings of the National Academy of Sciences* **108**, 12233–12237 (2011).
15. Keimer, B., Kivelson, S. A., Norman, M. R., Uchida, S. & Zaanen, J. From quantum matter to high-temperature superconductivity in copper oxides. *Nature* **518**, 179–186 (2015).
16. Xu, C. & Balents, L. Topological Superconductivity in Twisted Multilayer Graphene. *Physical Review Letters* **121** (2018).
17. Po, H. C., Zou, L., Vishwanath, A. & Senthil, T. Origin of Mott Insulating Behavior and Superconductivity in Twisted Bilayer Graphene. *Physical Review X* **8** (2018).
18. Koshino, M. *et al.* Maximally Localized Wannier Orbitals and the Extended Hubbard Model for Twisted Bilayer Graphene. *Physical Review X* **8** (2018).

19. Kang, J. & Vafeck, O. Symmetry, Maximally Localized Wannier States, and a Low-Energy Model for Twisted Bilayer Graphene Narrow Bands. *Physical Review X* **8** (2018).
20. Lian, B., Wang, Z. & Bernevig, B. A. Twisted Bilayer Graphene: A Phonon Driven Superconductor. *arXiv:1807.04382 [cond-mat]* (2018). ArXiv: 1807.04382.
21. Koshino, M. *et al.* Maximally localized wannier orbitals and the extended hubbard model for twisted bilayer graphene. *Phys. Rev. X* **8**, 031087 (2018).
22. Carr, S., Fang, S., Jarillo-Herrero, P. & Kaxiras, E. Pressure dependence of the magic twist angle in graphene superlattices. *Physical Review B* **98** (2018).
23. Chen, G. *et al.* Evidence of a gate-tunable Mott insulator in a trilayer graphene moir superlattice. *Nature Physics* **15**, 237–241 (2019).
24. Castro Neto, A. H., Guinea, F., Peres, N. M. R., Novoselov, K. S. & Geim, A. K. The electronic properties of graphene. *Reviews of Modern Physics* **81**, 109–162 (2009).
25. McCann, E. & Koshino, M. The electronic properties of bilayer graphene. *Reports on Progress in Physics* **76**, 056503 (2013).
26. Zhang, Y. *et al.* Direct observation of a widely tunable bandgap in bilayer graphene. *Nature* **459**, 820–823 (2009).
27. Zhang, Y.-H., Mao, D., Cao, Y., Jarillo-Herrero, P. & Senthil, T. Nearly flat Chern bands in moir superlattices. *Physical Review B* **99** (2019).
28. Chebrolu, N. R., Chittari, B. L. & Jung, J. Flatbands in twisted bi-bilayer graphene. *arXiv:1901.08420 [cond-mat]* (2019). ArXiv: 1901.08420.
29. Choi, Y. W. & Choi, H. J. Intrinsic Band Gap and Electrically Tunable Flat Bands in Twisted Double Bilayer Graphene. *arXiv:1903.00852 [cond-mat]* (2019). ArXiv: 1903.00852.
30. Cao, Y. *et al.* Superlattice-Induced Insulating States and Valley-Protected Orbita in Twisted Bilayer Graphene. *Physical Review Letters* **117** (2016).

31. Kim, K. *et al.* van der Waals Heterostructures with High Accuracy Rotational Alignment. *Nano Letters* **16**, 1989–1995 (2016).
32. Li, J. *et al.* Effective mass in bilayer graphene at low carrier densities: The role of potential disorder and electron-electron interaction. *Physical Review B* **94** (2016).
33. Sajadi, E. *et al.* Gate-induced superconductivity in a monolayer topological insulator. *Science* **362**, 922–925 (2018).
34. Fatemi, V. *et al.* Electrically tunable low-density superconductivity in a monolayer topological insulator. *Science* **362**, 926–929 (2018).
35. Ambegaokar, V. & Mermin, N. D. Thermal Anomalies of He 3 : Pairing in a Magnetic Field. *Physical Review Letters* **30**, 81–84 (1973).
36. Lee, J. Y. *et al.* Theory of correlated insulating behaviour and spin-triplet superconductivity in double twisted bilayer graphene. *To be posted* .
37. Julian, S. Viewpoint: Pairing with Spin Fluctuations. *Physics* **5** (2012).

Acknowledgements The major experimental work is supported by DOE (DE-SC0012260). P.K. acknowledges partial support from the Gordon and Betty Moore Foundation’s EPiQS Initiative through Grant GBMF4543 and the DoD Vannevar Bush Faculty Fellowship N00014-18-1-2877. A.V, J.Y.L and E.K were supported by a Simons Investigator Fellowship. K.W. and T.T. acknowledge support from the Elemental Strategy Initiative conducted by the MEXT, Japan, A3 Foresight by JSPS and the CREST (JPMJCR15F3), JST. A portion of this work was performed at the National High Magnetic Field Laboratory, which is supported by the National Science Foundation Cooperative Agreement No. DMR-1157490* and the State of Florida. Nanofabrication was performed at the Center for Nanoscale Systems at Harvard, supported in part by an NSF NNIN award ECS-00335765. We thank Shiang Fang, Stephen Carr, Yonglong Xie, Efthimios Kaxiras, Bertrand Halperin and Jonah Waissman for helpful discussion.

Competing Interests The authors declare that they have no competing financial interests.

Correspondence Correspondence and requests for materials should be addressed to X. Liu (email: xi-aomeng@princeton.edu) and P. Kim (email: philipkim@g.harvard.edu).

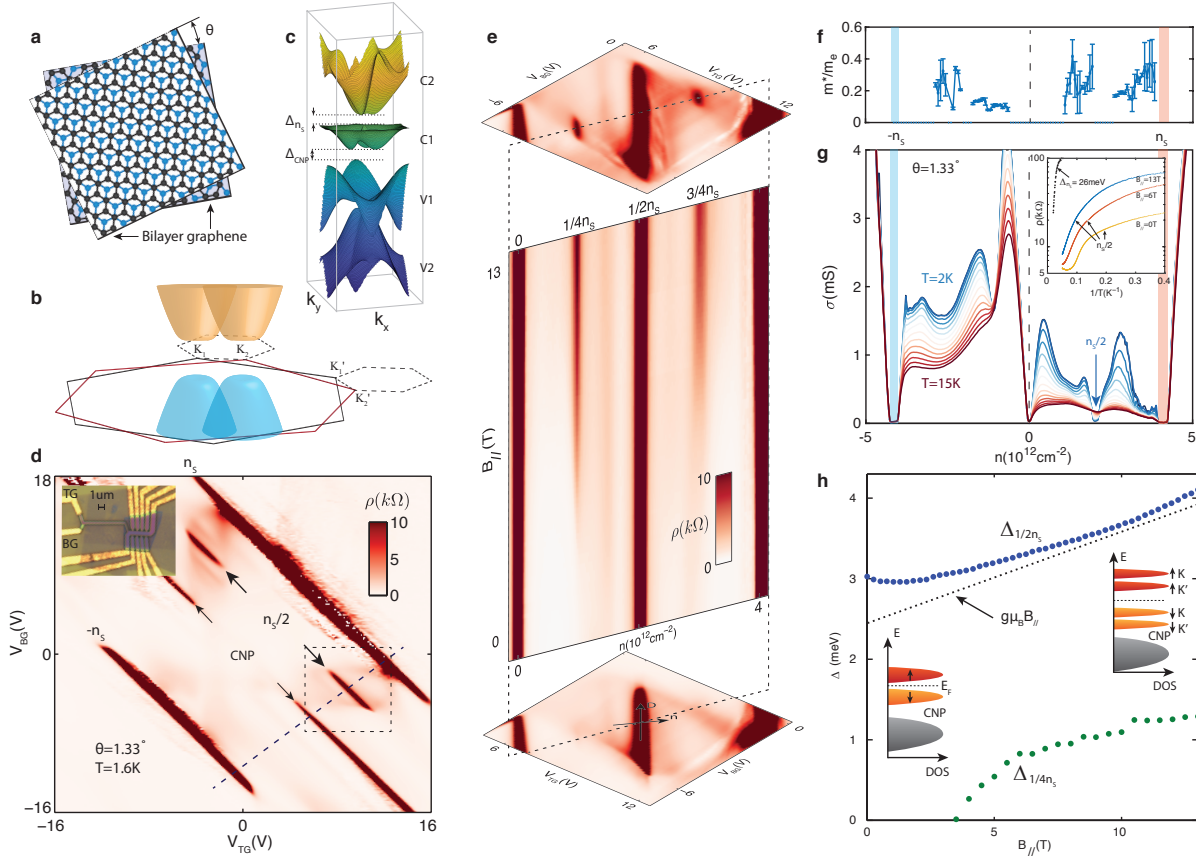


Figure 1: | **Half-filled and quarter-filled insulating states in $\theta = 1.33^\circ$ sample.** **a**, Schematic diagram of twisted bilayer-bilayer graphene with twist angle θ . **b**, Brillouin zone and band structure of the two individual bilayer graphene under perpendicular displacement field. The dashed hexagon represent mini-Brillouin zone of the moire superlattice. **c**, Calculated band structure for $\theta = 1.33^\circ$ TDBG at optimal displacement field D_m . **d**, Resistivity as a function of top and bottom gate voltages. Charge neutral point (CNP), full-filled band (n_s) and half-filled band ($n_s/2$) are marked. Inset, optical microscope image of the device. The leads for the top and bottom graphite gates are noted with TG and BG. **e**, Development of the insulating states with parallel magnetic fields. The top and bottom panels are zoom-in scans corresponding to areas marked by the dashed square in **d**. **g**, Conductivity as a function of density along the dashed line marked in **d** at various temperatures. Inset, Arrhenius plot for the full-filled insulating state (n_s) and half-filled insulating

state ($n_s/2$) under different parallel magnetic fields. **f**, Effective mass measured by temperature dependent quantum oscillations along the same line as **g**. **h**, Half-filled and quarter-filled insulating gaps as a function of parallel magnetic field. The dashed line indicates Zeeman energy with $g = 2$. Insets, Schematic diagram of density of states. The gray band represent v_1 , while the orange color represents spin-polarized half-filled c_1 band and red depicts the upper spin band of c_1 . Black arrows indicate the spin-polarization direction of the corresponding band. The orange and red bands are further split into four bands under strong parallel magnetic fields.

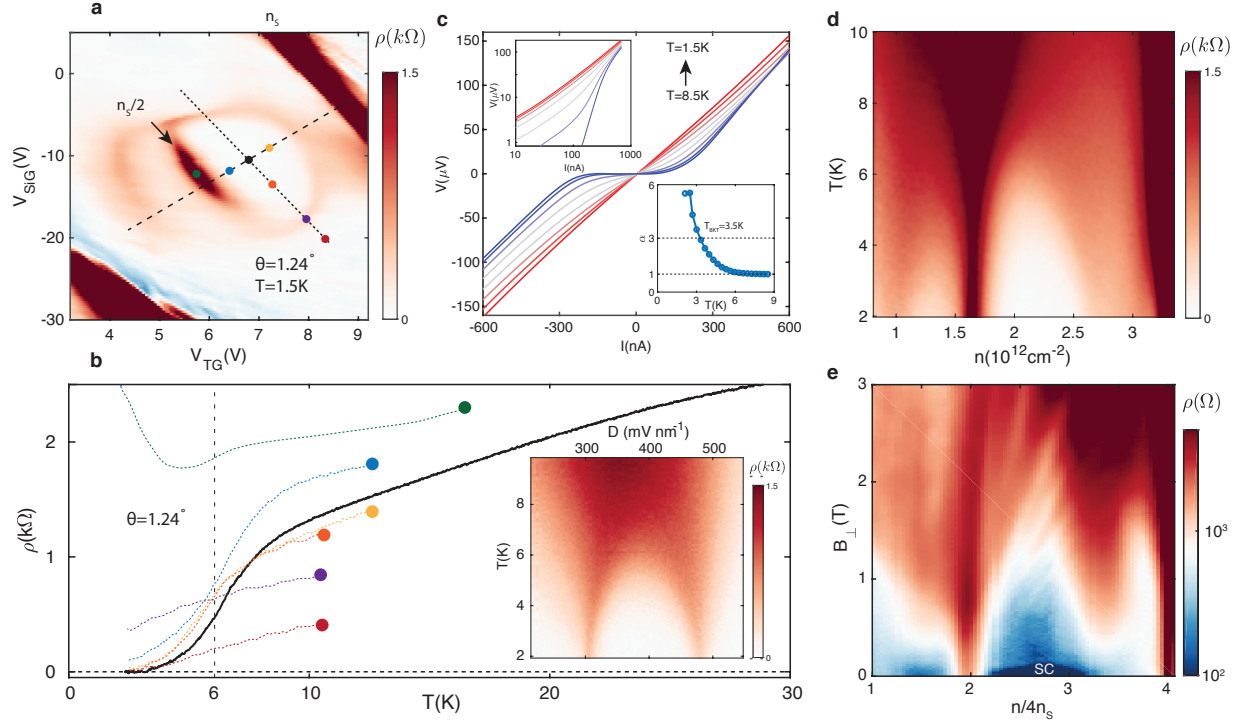


Figure 2: | **Superconductivity in 1.24° sample.** **a**, Resistivity map around the half-filled insulator and superconductor. **b**, Resistivity as a function of temperature at different spot marked by colored circles in **a** using the corresponding colors. Inset, temperature dependence along the constant density line-cut marked by dotted line in **a**. **c**, I - V curves at optimal doping n_m and displacement field D_m (black circle in Fig. 2a), Top left inset, I - V in log scale. Bottom right inset, power α ($V \propto I^\alpha$) as a function of temperature. **d**, Temperature dependence of the constant displacement field line-cut (dashed line in **a**). **e**, Perpendicular magnetic field dependence along the same line in **d** at $T = 1.5$ K.

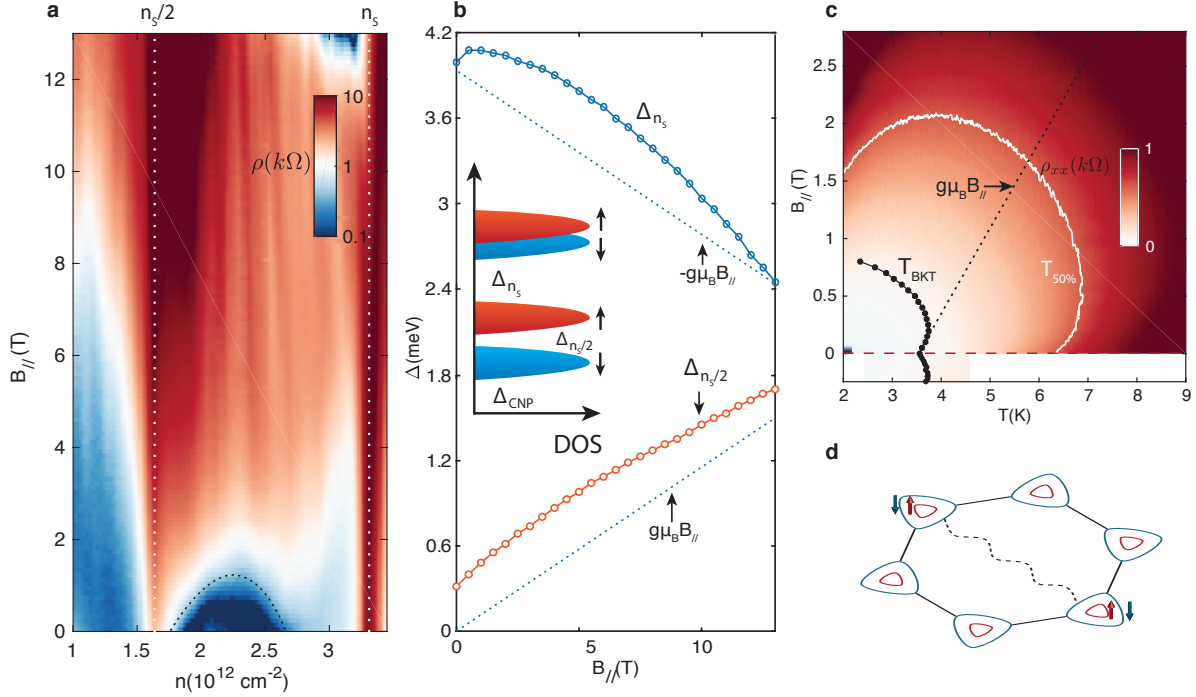


Figure 3: | Spin-polarized superconductivity. **a**, Parallel field dependence of resistivity along the same constant displacement field line as Fig. 2d and 2e. The color plot is in log scale, with superconducting region noted by dashed half-circle. **b**, Half-filling and full-filling gap as a function of parallel magnetic field in the $\theta = 1.24^\circ$ device. Dashed lines mark the Zeeman energy with $g = 2$ for comparison. **c**, Resistivity as a function of temperature and parallel magnetic field at the optimal doping n_m and displacement field D_m . The BKT temperature is overlaid on the graph (black circles and line). Red dashed line marks zero magnetic field, while black dotted line represents $k_B \Delta T_{BKT} \approx g\mu_B |B_{\parallel}|$. **d**, Illustration of possible ferromagnetic pairing mechanism. Pairing (as indicated by wavy dashed line) occurs between electrons in the opposite valleys with the same spin.

²₁ Supplementary Information

³ S1 Theoretical band structure of twisted bilayer-bilayer graphene

⁴ Fig. S1 shows the evolution of the moire band structure with increasing D . The band structure
⁵ of TDBG with ABAB stacking is obtained as the following. In TDBG, each bilayer graphene
⁶ has a tight-binding Bloch Hamiltonian at a momentum \mathbf{k} given by

$$H(\mathbf{k}) = \begin{pmatrix} U_1 + \Delta & -\gamma_0 f(\mathbf{k}) & \gamma_4 f^*(\mathbf{k}) & \gamma_1 \\ -\gamma_0 f^*(\mathbf{k}) & U_1 & \gamma_3 f(\mathbf{k}) & \gamma_4 f^*(\mathbf{k}) \\ \gamma_4 f(\mathbf{k}) & \gamma_3 f^*(\mathbf{k}) & U_2 & -\gamma_0 f(\mathbf{k}) \\ \gamma_1 & \gamma_4 f(\mathbf{k}) & -\gamma_0 f^*(\mathbf{k}) & U_2 + \Delta \end{pmatrix}, \quad (1)$$

⁷ which is labelled in the order of A_1 , B_1 , A_2 , B_2 sites. $f(\mathbf{k}) \equiv \sum_l e^{i\mathbf{k}\cdot\delta_l}$, where $\delta_1 = a(0, 1)$,
⁸ $\delta_2 = a(\sqrt{3}/2, -1/2)$, $\delta_3 = a(-\sqrt{3}/2, -1/2)$ with $a = 1.42$ Å. In particular, the electrostatic
⁹ energy difference U between top and bottom-most layers is important tuning parameter. With
¹⁰ this Hamiltonian, one can follow the continuum model approach in Ref. [2] to calculate the
¹¹ moire band structure.

¹² In the numerical simulation, we use phenomenological parameters

$$(\gamma_0, \gamma_1, \gamma_3, \gamma_4, \Delta) = (2.61, 0.361, 283, 138, 15) \text{ eV} \quad (2)$$

¹³ obtained from Ref. [1]. Compared to TBG, TDBG has additional parameters γ_1 , γ_3 (trigonal
¹⁴ warping), γ_4 (particle-hole asymmetry) and Δ on top of γ_0 (nearest-neighbor hopping). Al-
¹⁵ though small relative to γ_0 , these parameters are important to understand the experimental
¹⁶ data. Particularly, for zero U , γ_3 gives arise to larger bandwidth (no magic angle for TDBG)
¹⁷ and overlap between c_1 and v_1 . This is the reason why the system is metallic at CNP. Fur-
¹⁸ thermore, γ_4 and Δ give arise to the electron-hole asymmetry. Due to these terms, the band
¹⁹ isolation region for v_1 becomes much smaller than the band isolation region for c_1 . For the moire
²⁰ hopping parameters, $(w_0, w_1) = (0.08, 0.1)$ eV is used to account for the relaxation effect [3].

²¹ The relaxation increases the gap between c_1 and c_2 (v_1 and v_2), stabilizing the insulating states
²² for the range of D at $\nu = \pm 4$ fillings. For more details, See Ref. [4].

²³ **S2 Experimental displacement field range for isolated band, correlated ²⁴ insulator and superconductivity**

²⁵ Fig. S2 shows the experimental displacement field ranges where the correlated insulator, su-
²⁶ perconductivity and isolated band are observed. At a certain displacement field, isolated band
²⁷ refers to the coexistence of a bandgap between c_1 and c_2 as well as a bandgap between c_1 and
²⁸ v_1 . We can see the correlated insulators and superconductivity onset at the same displacement
²⁹ field as the band isolation develop but discontinue before the band isolation terminate at higher
³⁰ displacement field, suggesting their existence pose additional requirements on the band structure
³¹ other than just band isolation. This requirement is likely to be a narrow bandwidth.

³² **S3 Additional data of $\theta = 1.33^\circ$ sample**

³³ **S3.1 Temperature dependence of resistance around half-filling**

³⁴ Fig. S3 shows that next to the half filled insulator (line A), resistance drops as temperature
³⁵ decreases but levels off at lower temperatures and does not go superconducting (line B). It was
³⁶ checked down to 300mK with no superconducting transition observed in this $\theta = 1.33^\circ$ device.

³⁷ **S3.2 Landau Fan diagram**

³⁸ Under perpendicular magnetic field, clear fan can be identified coming from the charge neutral
³⁹ point, full filling $\pm n_S$ ($\approx 4.1 * 10^{12} cm^{-2}$) as well as half-filled electron band $n_S/2$. The fan
⁴⁰ from charge neutral point first develops with a degeneracy of four in the low field limit, which
⁴¹ is subsequently lifted at higher magnetic fields. On the contrary, fan from hall-filling start with
⁴² a degeneracy of two, which is consistent with the picture of a spin-polarized half-filled band.
⁴³ Interestingly, the sequence of these quantum oscillation is also unusual, such as $\nu = 3, 5, 7$,
⁴⁴ which are odd numbers. The reason for this is still unclear to us. At perpendicular magnetic

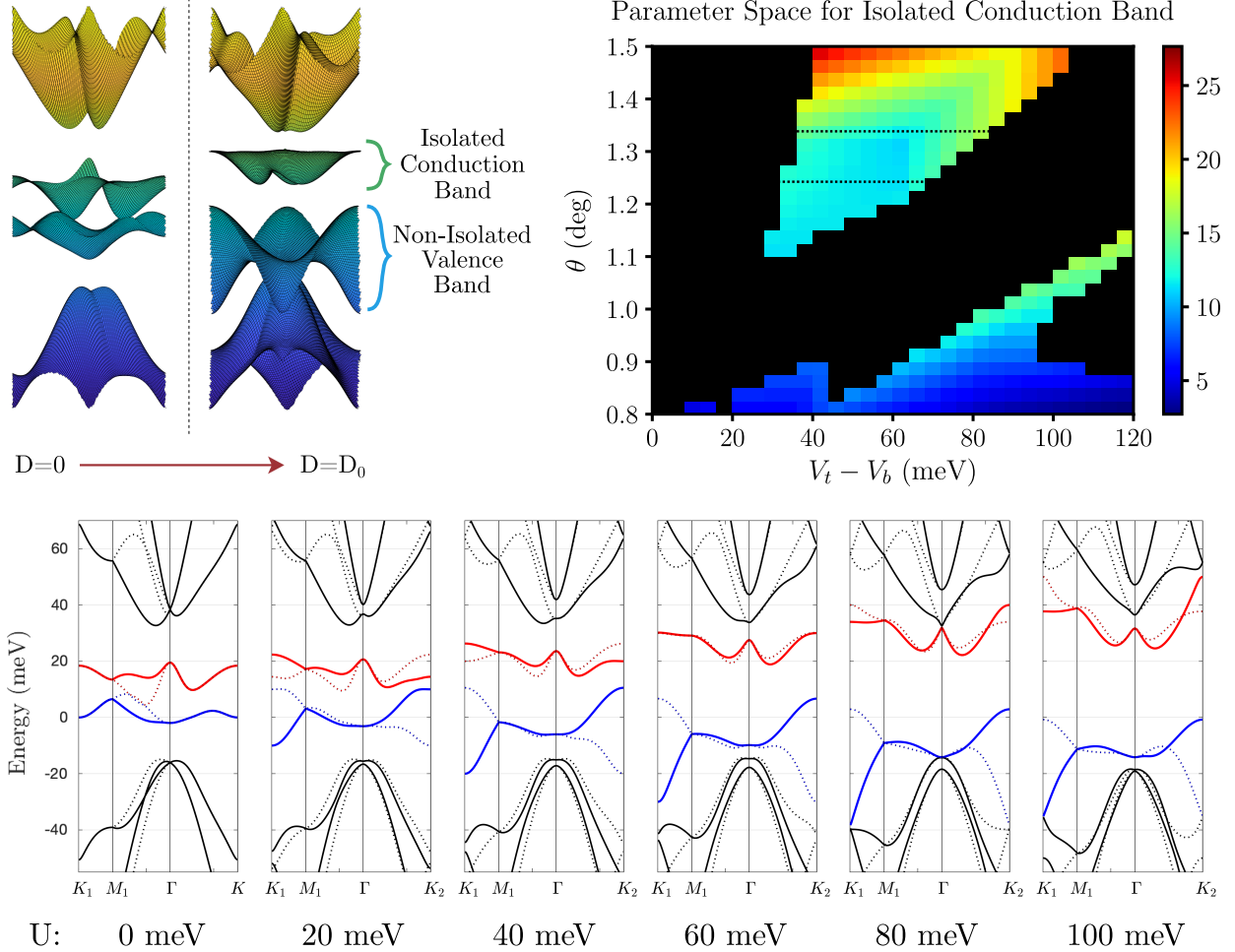


Figure S 1: (Top Left), calculated band structure of TBBG at zero displacement field and optimal displacement field D_m for the isolated flat band. (Top Right), calculated parameter space for isolated conduction band (x-axis is onsite potential difference $U = V_t - V_b$ between the top and bottom bilayer graphene, y-axis is twist angle). Color represent bandwidth of the first conduction band c_1 (meV). In the colored parameter space, c_1 is isolated from the remote band and valance bands. Dotted line represents cuts at $\theta = 1.24, 1.33^\circ$, corresponding to Fig. 2. (Bottom), band structures at $\theta = 1.24^\circ$ for increasing U . Color: red for c_1 and blue for v_1 . Dotted lines are for bands in the other valley.

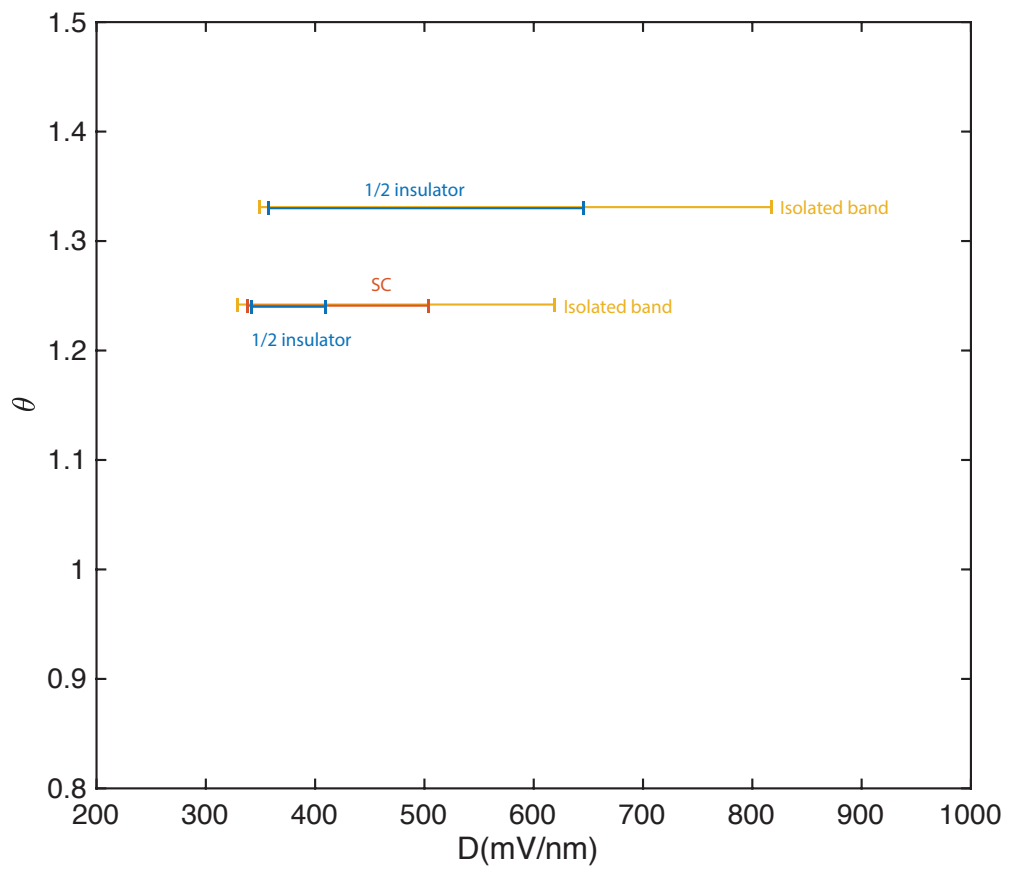


Figure S 2: Displacement field ranges for different features observed in the two different twist angle samples.

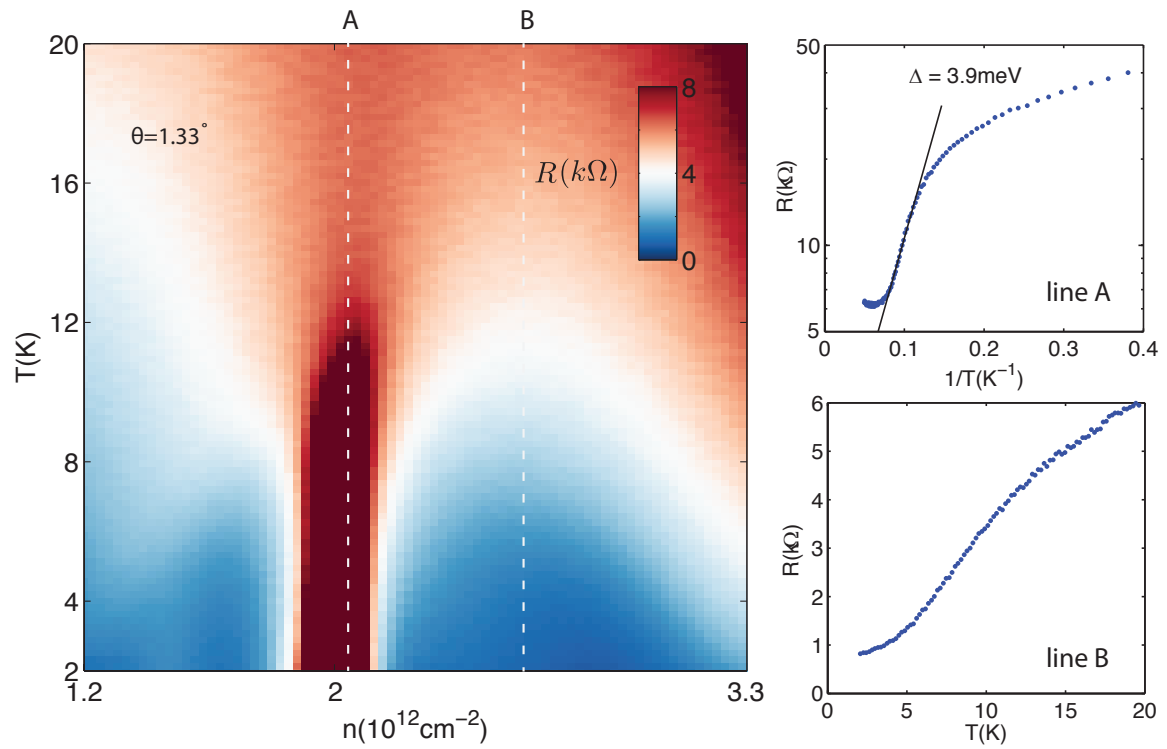


Figure S 3: Resistance as a function of density and temperature in $\theta = 1.33^\circ$ device. Line A cut through the half-filled insulator. Line B cut through a low resistance area next to the half-filled insulator, which shows dropping resistance as temperature decreases but does not go to zero.

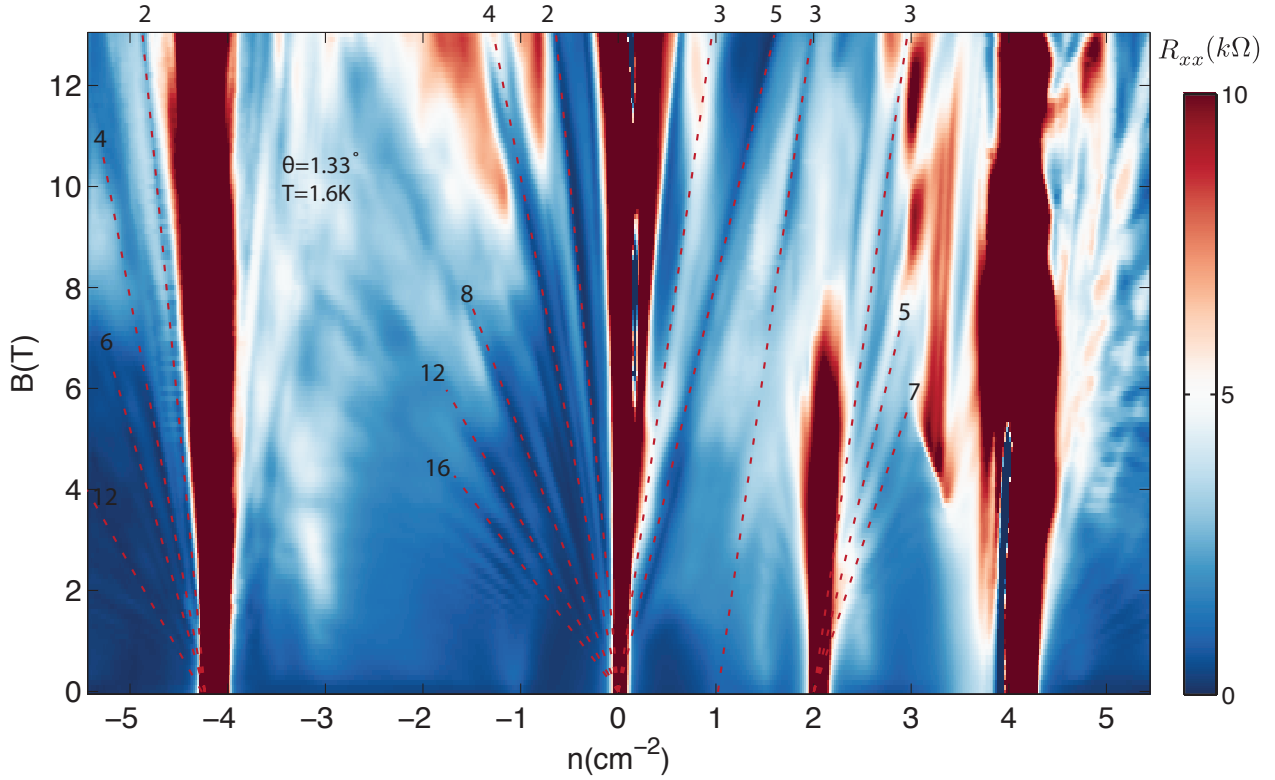


Figure S 4: Fan diagram of longitudinal resistance as a function of density and perpendicular magnetic field. The numbers in the plot indicate Landau level degeneracy corresponding to the lines next to them

45 field above 7T, the half filled insulator disappears, presumably due to the orbit effect of the
 46 perpendicular magnetic field.

47 **S3.3 Effective mass calculation**

48 We calculate the effective cyclotron mass from temperature dependent magnetoresistance (SdH)
 49 oscillations. The cyclotron mass is a measure of the density of state and thus directly related
 50 to the Landau level separation (cyclotron gap) at a given magnetic field. As temperature rises,
 51 SdH oscillation amplitude is reduced when the temperature is comparable with the cyclotron
 52 gap as: $\Delta R \propto \chi / \sinh(\chi)$ in which $\chi = 2\pi^2 k T m^* / \hbar e B$.

53 We measured SdH oscillation at all densities between filling factor $n/n_S = -4$ and 4, at
54 $T=0.3, 2, 3, 4, 6, 9, 14\text{K}$ (example: Fig. S5a-c). We then extract the oscillation amplitude
55 and plot the oscillation amplitude as a function of temperature over magnetic field at which the
56 oscillation amplitude was extracted. Fitting this with the above formula in the last paragraph
57 produces the effective cyclotron mass shown in main text.

58 **S3.4 Perpendicular magnetic field effect on the half-filled insulating state**

59 As shown in Fig. S4, the half filled insulator disappeared above perpendicular magnetic field of
60 7T . However, below this critical field, the displacement field range where the half-filled insulator
61 resides remain the same as zero magnetic field, as demonstrated by Fig. S6.

62 **S4 Large twist angle $\theta = 2^\circ$ sample**

63 In the larger twist angle samples ($\theta = 1.9^\circ$ and 2°), we do not observe sign of correlated insulator
64 or superconductor (Fig. S7). And isolated conduction and valance band persist over most of
65 the displacement field range. At zero displacement field, there is a gap between conduction and
66 valance band, which closes and reopens as displacement field increases. This is confirmed from
67 the numerics as well. The absence of correlated insulator state is presumably due to the absence
68 of flat band (numerically calculated bandwidth is about 80 meV), though no direct evidence
69 was obtained. Under small perpendicular magnetic field (1T), a resistance bump appears near
70 half-filling in the valance band but do not becomes fully insulating.

71 **S5 Additional data for $\theta = 1.24^\circ$ sample**

72 **S5.1 Resistivity over full gate range**

73 Fig. S8 shows resistivity measured over a larger gate voltage range for the $\theta = 1.24^\circ$ sample.
74 The silicon gate is used as the bottom gate here as this specific device does not have a graphite
75 bottom gate. The lack of symmetry between the top graphite gate and silicon gate are likely
76 caused by bad contact occurs when top gate voltage is negative (pn junction at the contact).

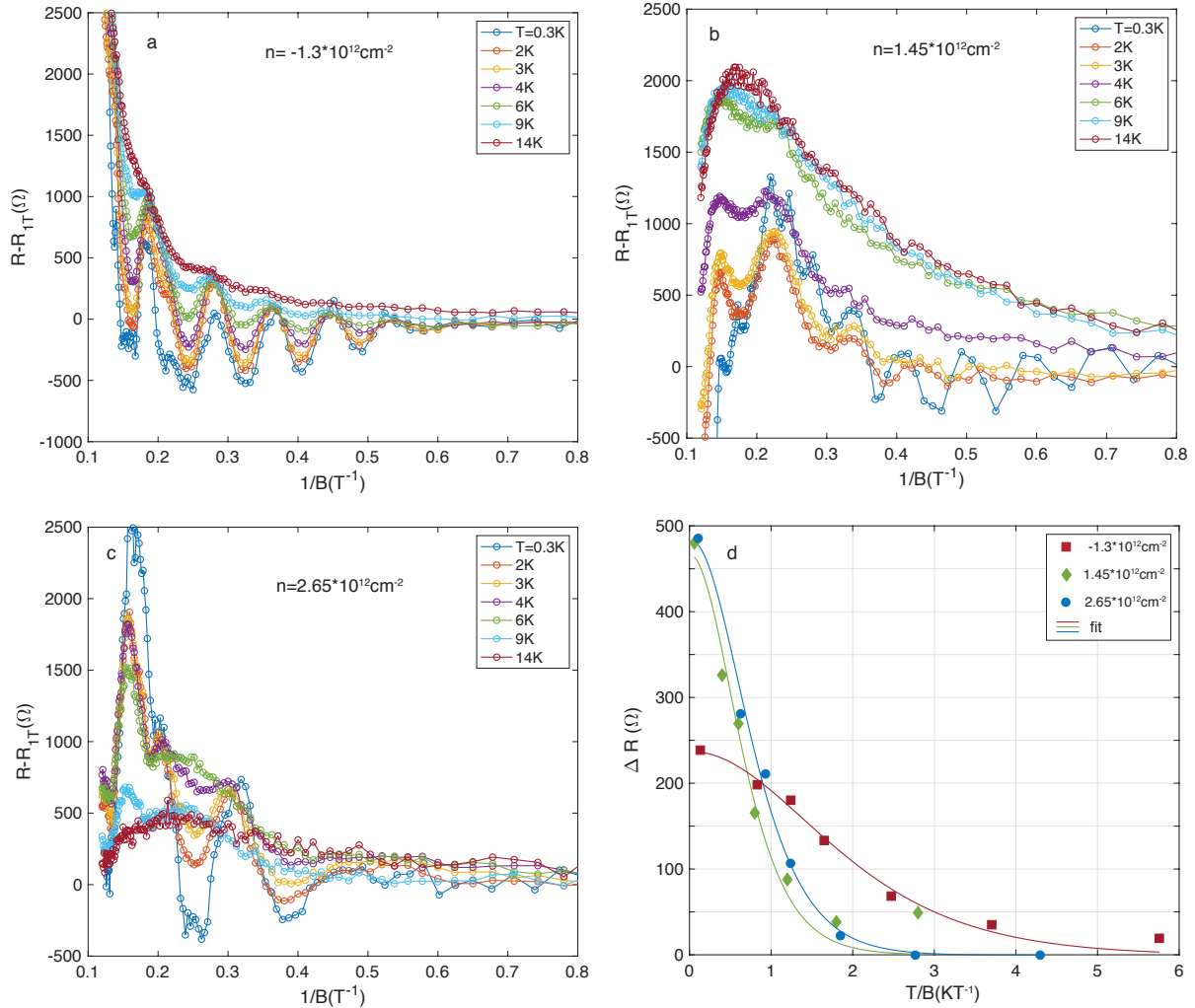


Figure S 5: Effective mass calculation. a-c, temperature dependent SdH oscillations at a few representative density points: a, in the valance band, b, in the conduction band below half filling, c, in the conduction band above half filling. d, extracted oscillation amplitude as a function of T/B for the points shown in a-c with curve fit.

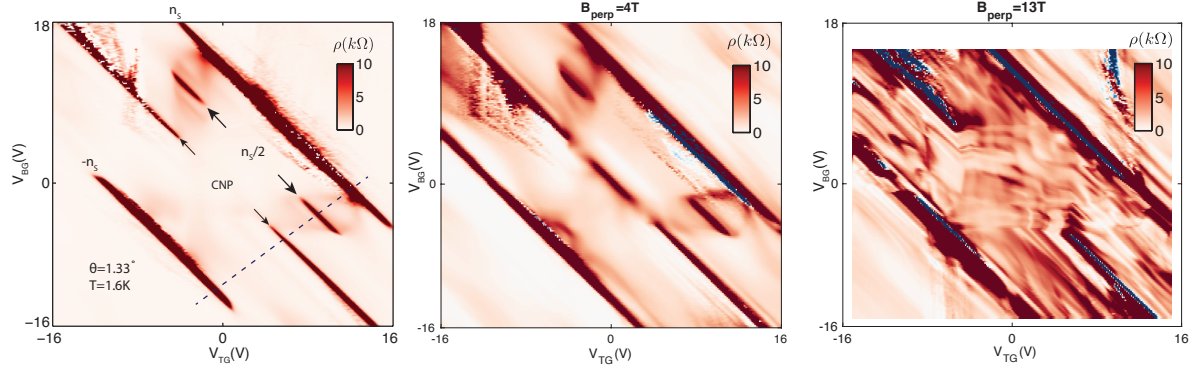


Figure S 6: Resistivity map as a function of top and bottom gate voltages under perpendicular magnetic fields of 0T (left), 4T (middle) and 13T (right). At 4T, the position of half-filled insulator remains the same as zero magnetic field.

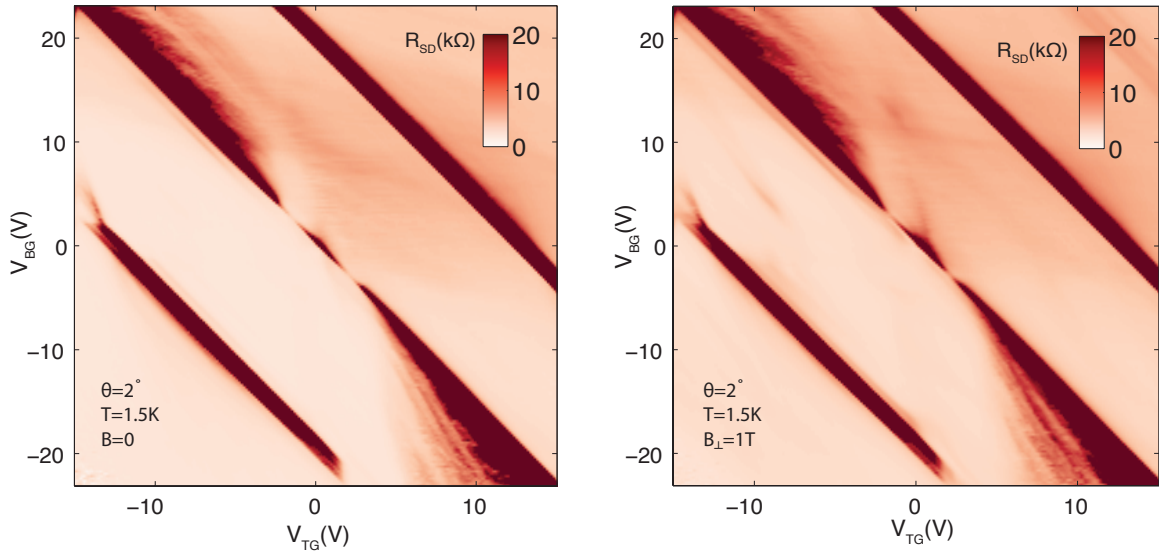


Figure S 7: Left, dual gate dependence of two terminal resistance under zero magentic field. Right, same measurement as left but under perpendicular magnetic field of 1T.

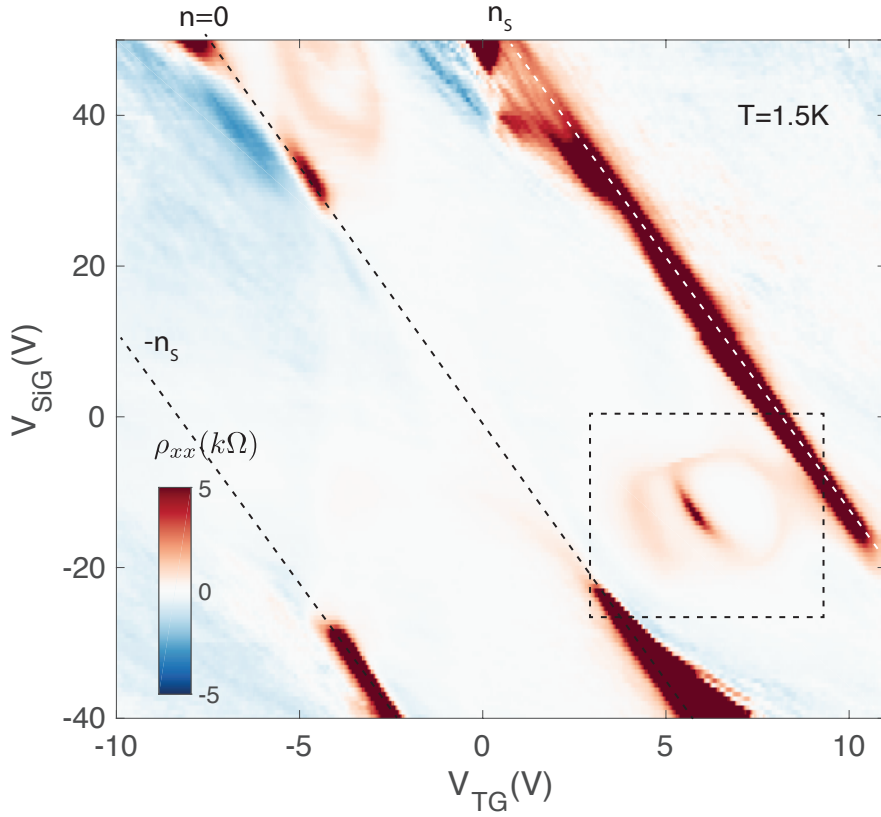


Figure S 8: Resistivity over a large range of gate voltages in the $\theta = 1.24^\circ$ sample. The dashed rectangle marks the zoomed-in scan shown in the main text Fig.2a

⁷⁷ This can be inferred from the negative resistivity with large noise when the top gate voltage is
⁷⁸ below -5V.

⁷⁹ **S5.2 Transport behavior outside superconducting ring**

⁸⁰ The temperature dependence of resistivity outside the superconducting ring lacks a critical
⁸¹ behavior (curve 1-4 in Fig. S9). Instead of a sharp superconducting transition observed inside
⁸² the ring (curve 6-8 in Fig. S9), the resistivity increases roughly linearly with temperature.
⁸³ As the displacement field move away from the ring, the temperature dependence become even
⁸⁴ weaker (curve 1 in Fig. S9). One probably cause of this low resistivity behavior is ballistic
⁸⁵ transport. As the displacement field deviate from the flat band condition, ballistic transport

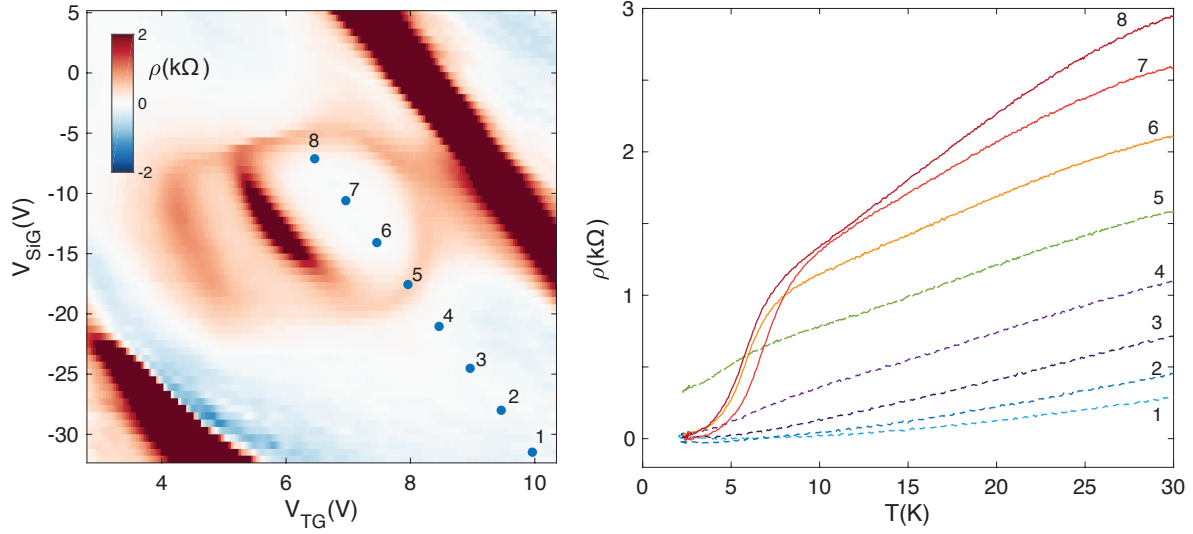


Figure S 9: Temperature dependence of resistivity at different gate configurations. Left, dual gate map showing the gate voltage configuration of curve 1-8. Right, resistivity as a function of temperature measured at the spot marked by 1-8 in left figure. Curve 5 is on the boundary of the superconducting ring, while 1-4 is outside and 6-8 is inside.

could occur similar to that in a single bilayer graphene. As temperature rise, electron-phonon scattering causes the resistivity to increase gradually.

The lack of superconductivity outside of the ring can also be seen from the I - V curves. In Fig. S10, the left curve is taken inside the superconducting circle, which shows a typical superconducting I - V character. However, outside the circle, the four terminal voltage is symmetric over positive and negative current. This is unusual and cannot be associated with a superconducting transition. It may be cause by ballistic transport but we do not have further understanding of this rectifying behavior.

94 S5.3 Fan diagram and superconducting critical field under perpendicular magnetic 95 field

Fig. S11 shows the perpendicular field dependence of the $\theta = 1.24^\circ$ sample. According the BKT transition temperature, the perpendicular critical field is $\approx 0.1T$. The Landau level degeneracy

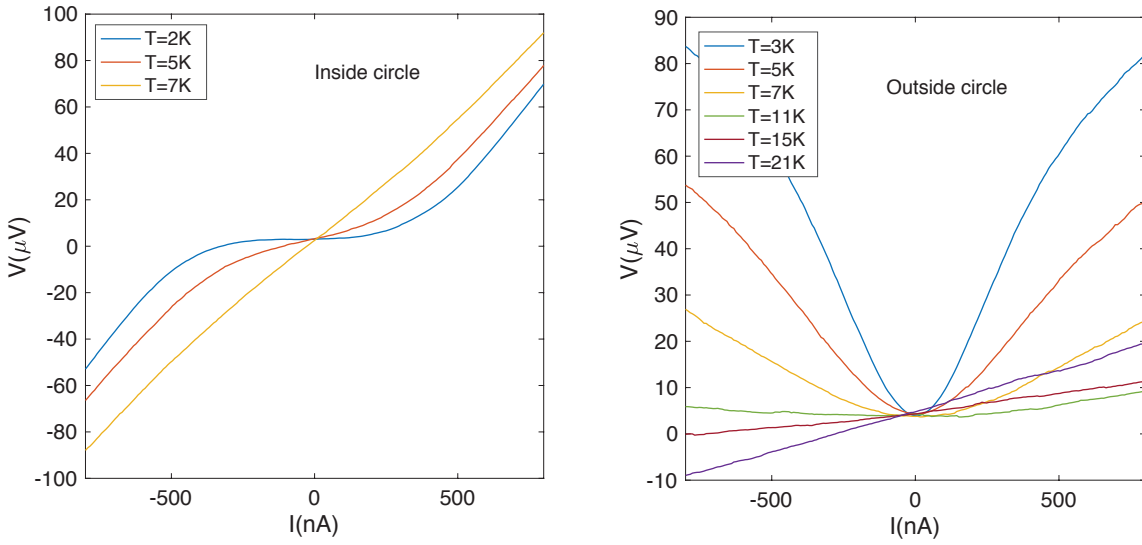


Figure S 10: I - V character inside (left) and outside (right) the superconducting ring.

98 of fan diagram coming from $n_s/2$ is 4.

99 **S5.4 Superconductor-insulator transition inducted by parallel magnetic fields**

100 Fig. S12 shows the temperature dependence of the resistivity in the superconducting phase at
 101 optimal doping n_m and displacement field D_m under different parallel magnetic fields B_{\parallel} . At zero
 102 B_{\parallel} , we can see the superconducting transition. However, as B_{\parallel} increases, the low-temperature
 103 behavior of resistance gradually becomes that of an insulator, with resistivity going down as
 104 temperature goes up. At $B_{\parallel} = 13T$, the low-temperature resistance is as high as $5.6k\Omega$. These
 105 behaviors suggest a possible superconductor-insulator transition induced by parallel magnetic
 106 field.

107 Furthermore, fig. S11 shows I-V curves at the same doping and displacement field. As
 108 parallel field increases, the critical current goes to zero, and V starts to increase linearly with I .
 109 Under even higher parallel fields, a insulating I-V becomes prominent, with differential resistance
 110 decreases as current increases.

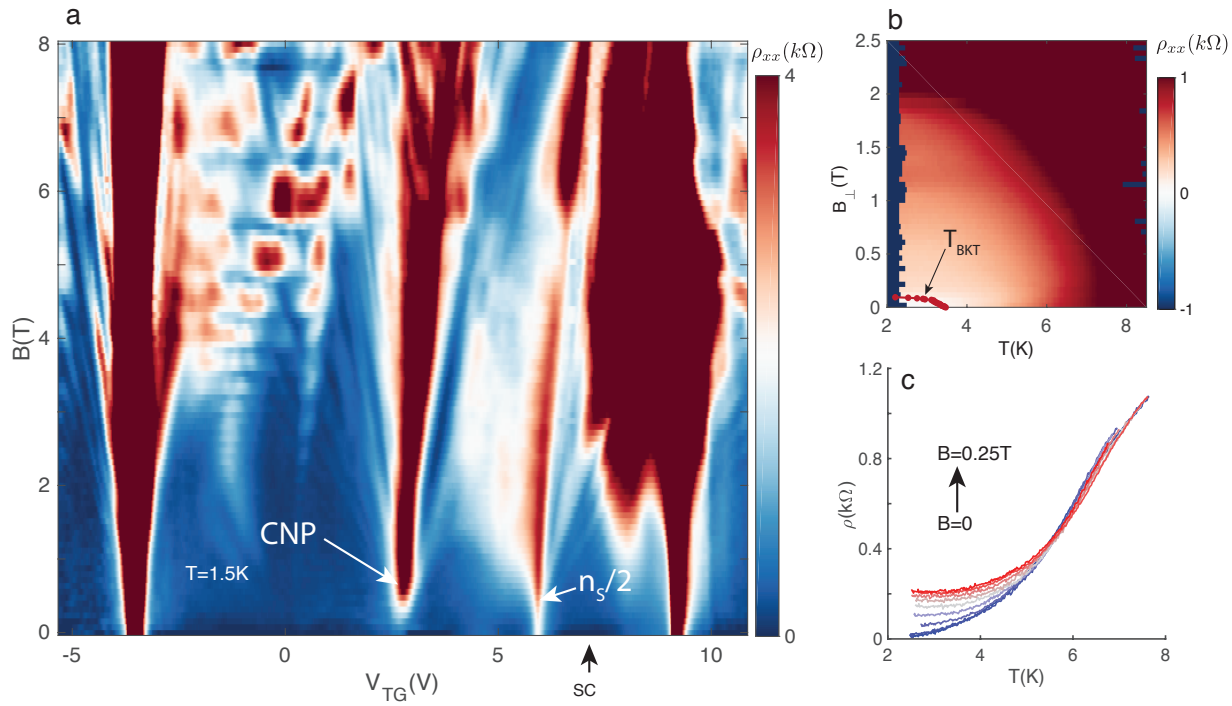


Figure S 11: Fan diagram and critical perpendicular magnetid field. a, Fan diagram of the $\theta = 1.24^\circ$ sample. The clear Hofstadter butterfly features are used to obtain the twisted angle in this sample. b, perpendicular magnetic field dependence of the superconducting transition at the optimal doping and displacement field. Red curve over-lapped on color plot shows the BKT transition temperature obtained from I - V characters. c, resistivity vs. temperature at different perpendicular fields between zero and 0.25T.

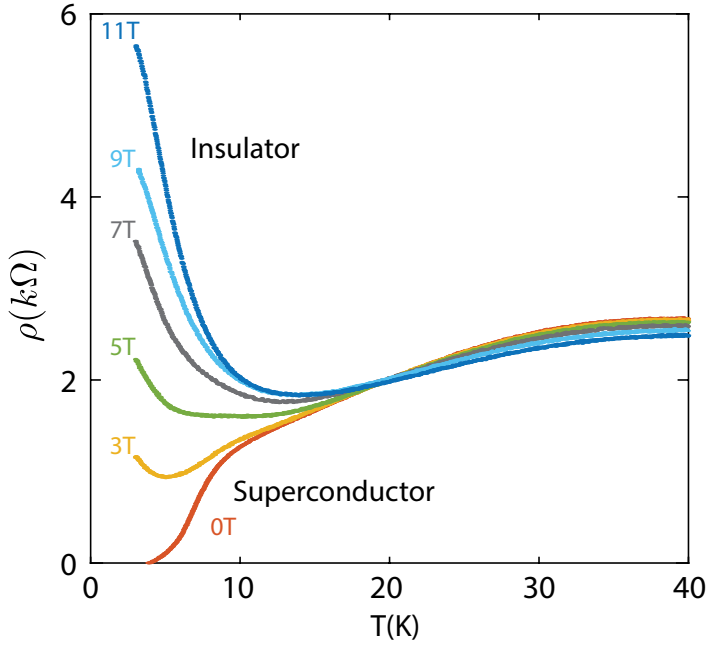


Figure S 12: Temperature dependence of the resistivity at optimal doping n_m and displacement field D_m under different parallel magnetic fields

¹¹¹ **S5.5 Additional evidences of parallel magnetic field enhancing superconductivity**

¹¹² We conducted some more analysis to demonstrate the enhancement of the superconductivity
¹¹³ due to parallel magnetic field. Fig. S14 shows a typical resistance v.s temperature profile in
¹¹⁴ the superconducting phase. We can define several temperature scales from the R v.s T curve.
¹¹⁵ For example, we can draw a tangent line at the point where the slope of the RT curve is the
¹¹⁶ largest, and we can extract the x-intercept of the tangent line and define $T_{intercept}$, which shows
¹¹⁷ a non-monotonic behavior similar to $T_{50\%}$ and T_{BKT} .

¹¹⁸ We can also measure dV/dI curves under different parallel fields. Fig. S15 shows clearly
¹¹⁹ that the critical current becomes larger as parallel field increases. This is another evidence that
¹²⁰ the superconductivity is strengthened by a small parallel magnetic field.

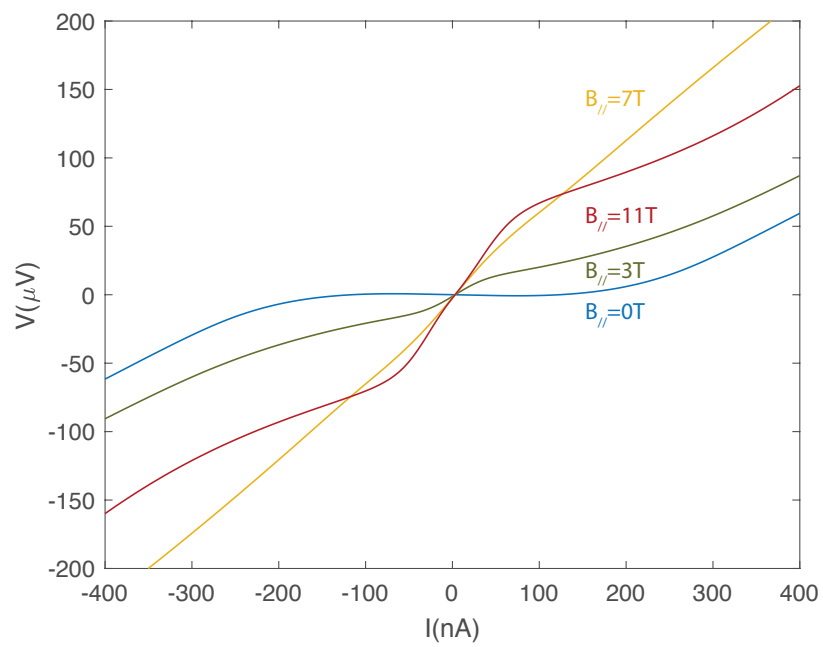


Figure S 13: I-V curves at optimal doping n_m and displacement field D_m under different parallel magnetic fields

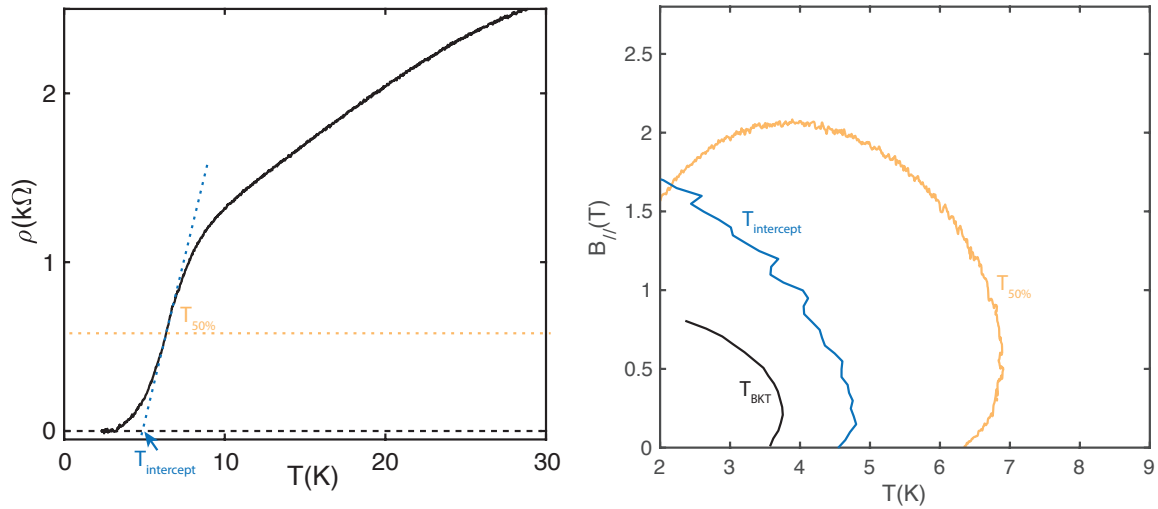


Figure S 14: Critical temperature defined by different metrics. Left, a typical resistivity curve. Right, different critical temperatures as a function parallel magnetic field.

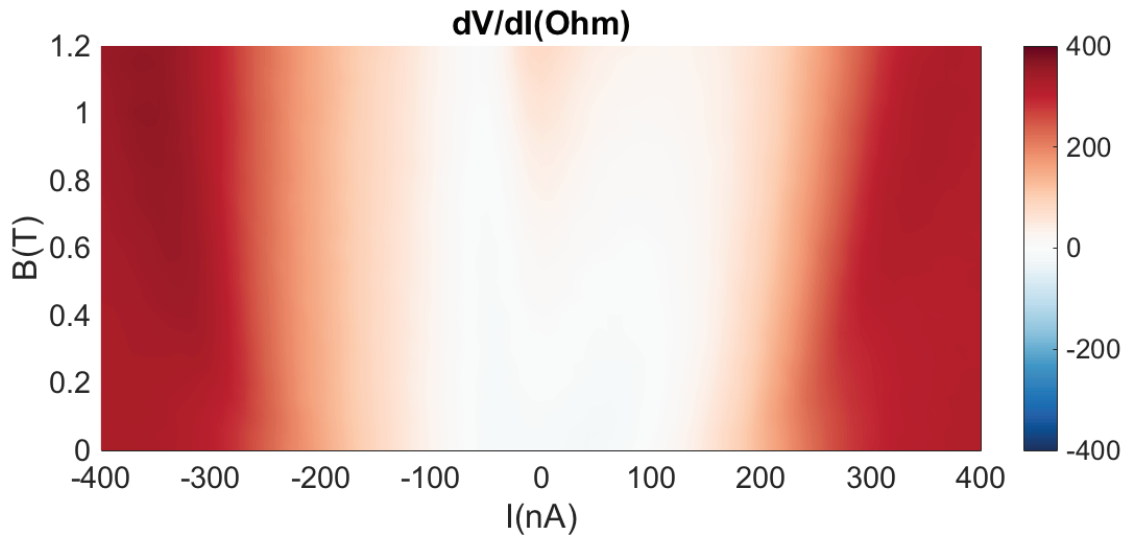


Figure S 15: Differential resistance as a function of current and parallel magnetic field. The current at which resistivity start to increase (critical current) is enhanced by the parallel magnetic field, as can be seen from the evident inverse bell shape. At even larger fields, a resistivity peak develops at zero bias current, terminating the superconductivity.

₁₂₁ **References**

₁₂₂ [1] Jung, Jeil and MacDonald, Allan H. *Phys. Rev. B* **89**, 035405 (2014).

₁₂₃ [2] Bistritzer, Rafi and MacDonald, Allan H. *Proceedings of the National Academy of Sciences*
₁₂₄ **108**, 12233–12237 (2011).

₁₂₅ [3] Moon, Pilkyung and Koshino, Mikiton *Phys. Rev. B* **87**, 205404 (2013).

₁₂₆ [4] Jong Yeon Lee, Eslam Khalaf, Shang Liu, Xiaomeng Liu, Zeyu Hao, Philip Kim, Ashvin
₁₂₇ Vishwanath *Theory of correlated insulating behaviour and spin-triplet superconductivity in*
₁₂₈ *double twisted bilayer graphene. To be posted* (2019)